SUPPORTING INFORMATION for

Influence of Active Site Location on Catalytic Activity in *de Novo*-Designed Zinc Metalloenzymes

Melissa L. Zastrow and Vincent L. Pecoraro*

Department of Chemistry, University of Michigan, Ann Arbor, Michigan 48109, United States

Contents

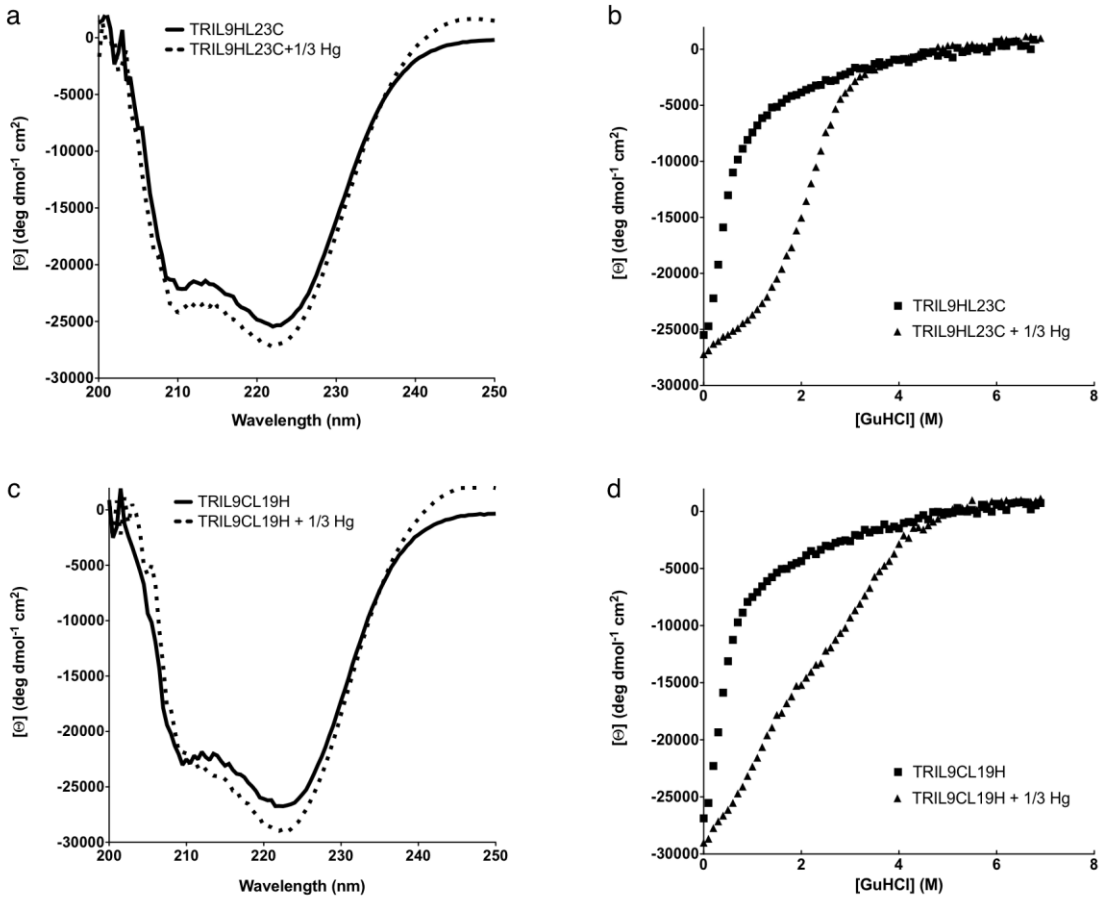

Figure S1. Folding of (**TRI**L9HL23C)$_3^{3-}$ (apo and +1/3 Hg(II)) and (**TRI**L9CL19H)$_3^{3-}$ (apo and +1/3 Hg(II)) as monitored by circular dichroism. a) CD spectra of (**TRI**L9HL23C)$_3^{3-}$ and (**TRI**L9HL23C)$_3^{3-}$ + 1/3 Hg(II) at pH 8.5 and 25°C. The molar ellipticities [Θ] at 222 nm are -25501 and -27210° dmol^{-1} cm^2, respectively. b) Guanidine hydrochloride denaturation titrations represented by the molar ellipticity values [Θ] at 222 nm vs denaturant concentration for (**TRI**L9HL23C)$_3^{3-}$ and (**TRI**L9HL23C)$_3^{3-}$ + 1/3 Hg(II). c) CD spectra of (**TRI**L9CL19H)$_3^{3-}$ and (**TRI**L9CL19H)$_3^{3-}$ + 1/3 Hg(II) at pH 8.5 and 25°C. The molar ellipticities [Θ] at 222 nm are -26872 and -29002° dmol^{-1} cm^2, respectively. d) Guanidine hydrochloride denaturation titrations represented by the molar ellipticity values [Θ] at 222 nm vs denaturant concentration for (**TRI**L9CL19H)$_3^{3-}$ and (**TRI**L9CL19H)$_3^{3-}$ + 1/3 Hg(II). As for our previously reported His-containing **TRI** peptides, we have not reported a quantitative determination of free energy values because the denaturation curves for these peptides do not level off at zero concentration of denaturant.[1]

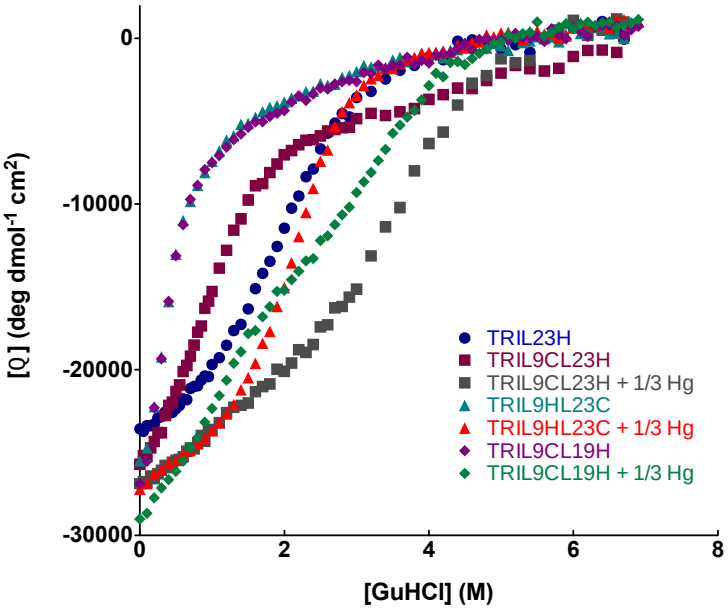

Figure S2. Comparison of the unfolding of (**TRI**L9HL23C)$_3^{3-}$ (apo and +1/3 Hg(II)) and (**TRI**L9CL19H)$_3^{3-}$ (apo and +1/3 Hg(II)) to (**TRI**L23H)$_3$ and (**TRI**L9CL23H)$_3^{3-}$ (apo and +1/3 Hg(II))[1]. Guanidine hydrochloride denaturation titrations at pH 8.5 represented by the molar ellipticity values [Θ] at 222 nm vs denaturant concentration for (**TRI**L23H)$_3$, (**TRI**L9CL23H)$_3^{3-}$, (**TRI**L9HL23C)$_3^{3-}$, and (**TRI**L9CL19H)$_3^{3-}$. For each of the Cys-containing peptides, when comparing the apo versions and the Hg(II)-bound peptides, the midpoint is shifted to a higher denaturant concentration, demonstrating that the structural site confers stability on each of the constructs.

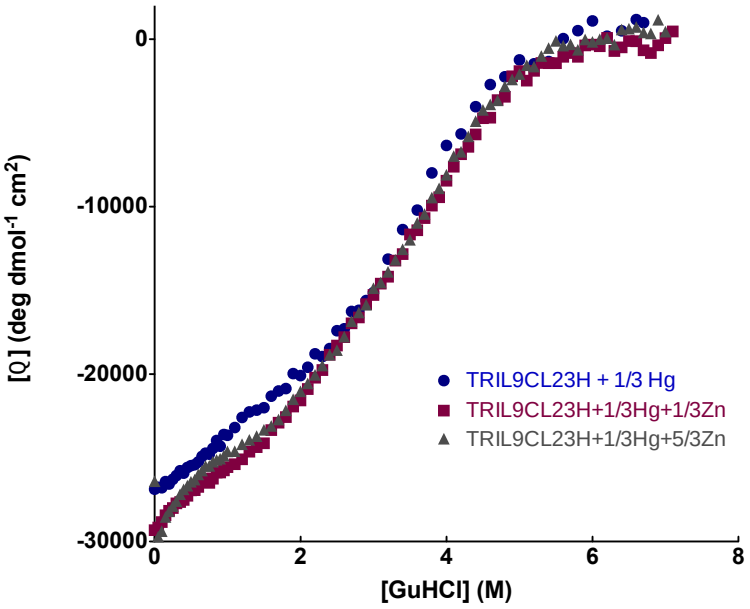

Figure S3. Comparison of the unfolding of (**TRI**L9CL23H)$_3^{3-}$ +1/3 Hg(II) in the presence of 0, 1, and 5 equivalents of Zn(II).[1] Guanidine hydrochloride denaturation titrations at pH 8.5 represented by the molar ellipticity values [Θ] at 222 nm vs denaturant concentration for (**TRI**L9CL19H)$_3^{3-}$ +1/3 Hg(II) (●)[1], (**TRI**L9CL19H)$_3^{3-}$ +1/3 Hg(II) +1/3 Zn(II) (■), and (**TRI**L9CL19H)$_3^{3-}$ +1/3 Hg(II) +5/3 Zn(II) (▲). There is no shift in the midpoint of unfolding in the presence of Zn(II).

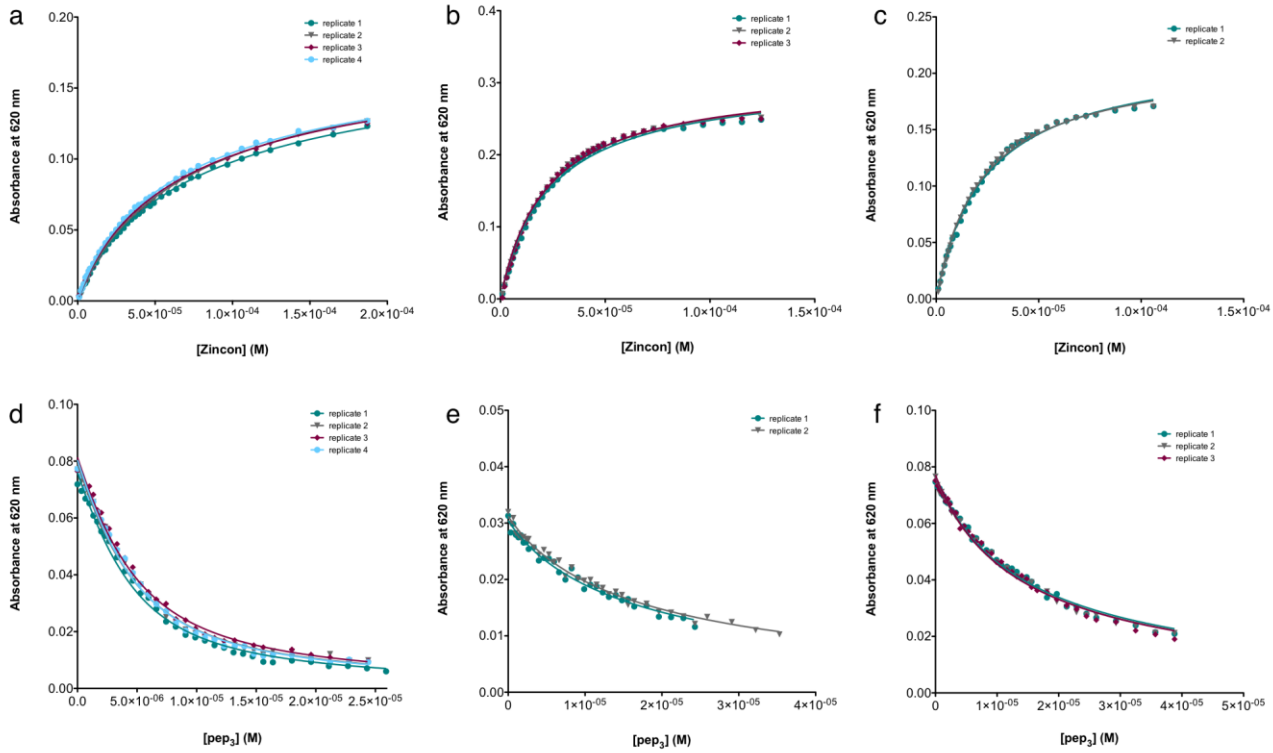

Figure S4. Competitive titrations against Zincon at pH 7.5 for (**TRI**L2WL23H)$_3$, [Hg(II)]$_S$(**TRI**L9HL23C)$_3^-$, and [Hg(II)]$_S$(**TRI**L9CL19H)$_3^-$. Plots of absorbances at 620 nm vs [Zincon] for the forward titrations of a) (**TRI**L2WL23H)$_3$, b) [Hg(II)]$_S$(**TRI**L9HL23C)$_3^-$, and c) [Hg(II)]$_S$(**TRI**L9CL19H)$_3^-$ and vs [pep$_3$] for the reverse titrations of d) (**TRI**L2WL23H)$_3$, e) [Hg(II)]$_S$(**TRI**L9HL23C)$_3^-$, and f) [Hg(II)]$_S$(**TRI**L9CL19H)$_3^-$.

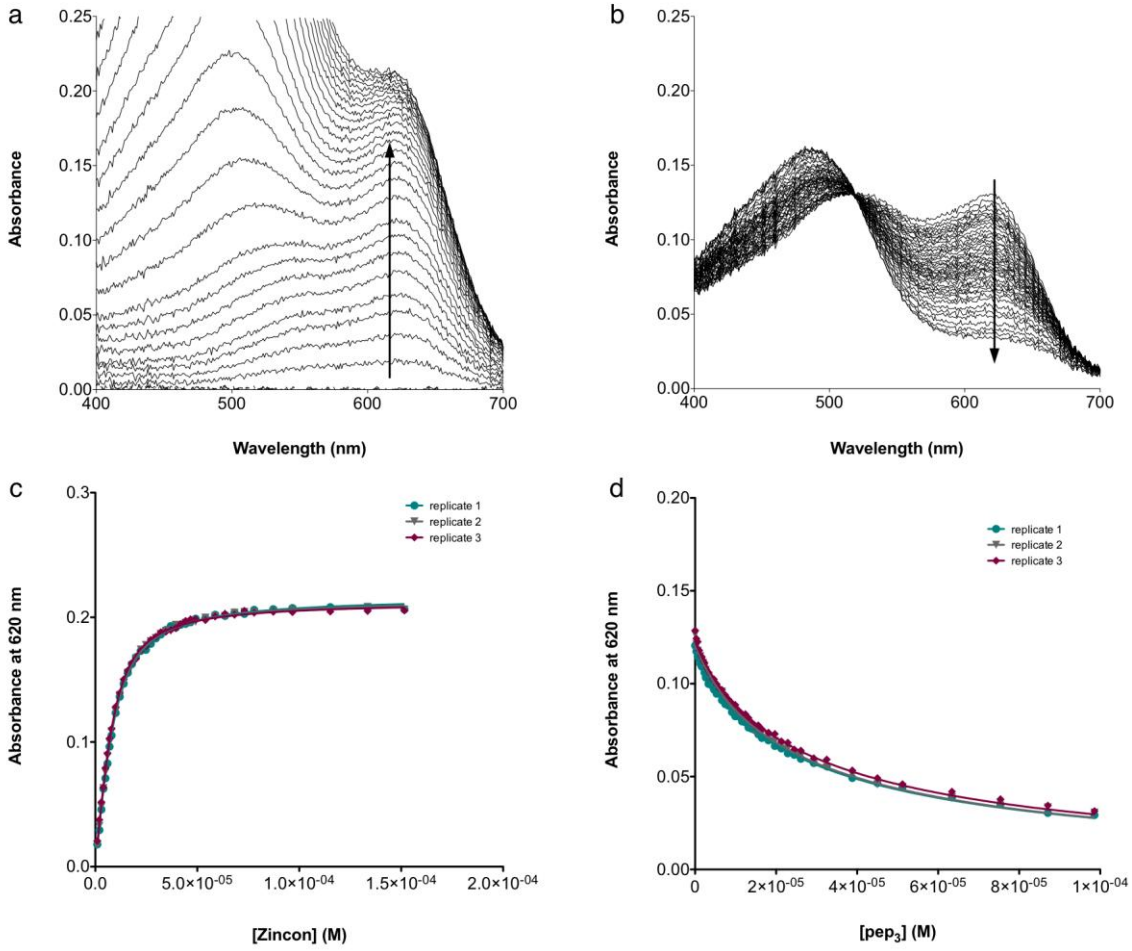

Figure S5. Competitive Zincon binding titrations at pH 9.0 for $[Hg(II)]_5$(**TRI**L9CL23H)$_3^-$ in the forward ($Zn(II)pep_3$ + Zincon) and reverse (Zn(II)Zi + pep_3) direction. a) Representative UV-visible spectra for the titration in the forward direction and b) in the reverse direction. c) Plot of absorbance at 620 nm as a function of increasing [Zincon] for the forward titration and d) as a function of increasing [pep_3] for the reverse titration.

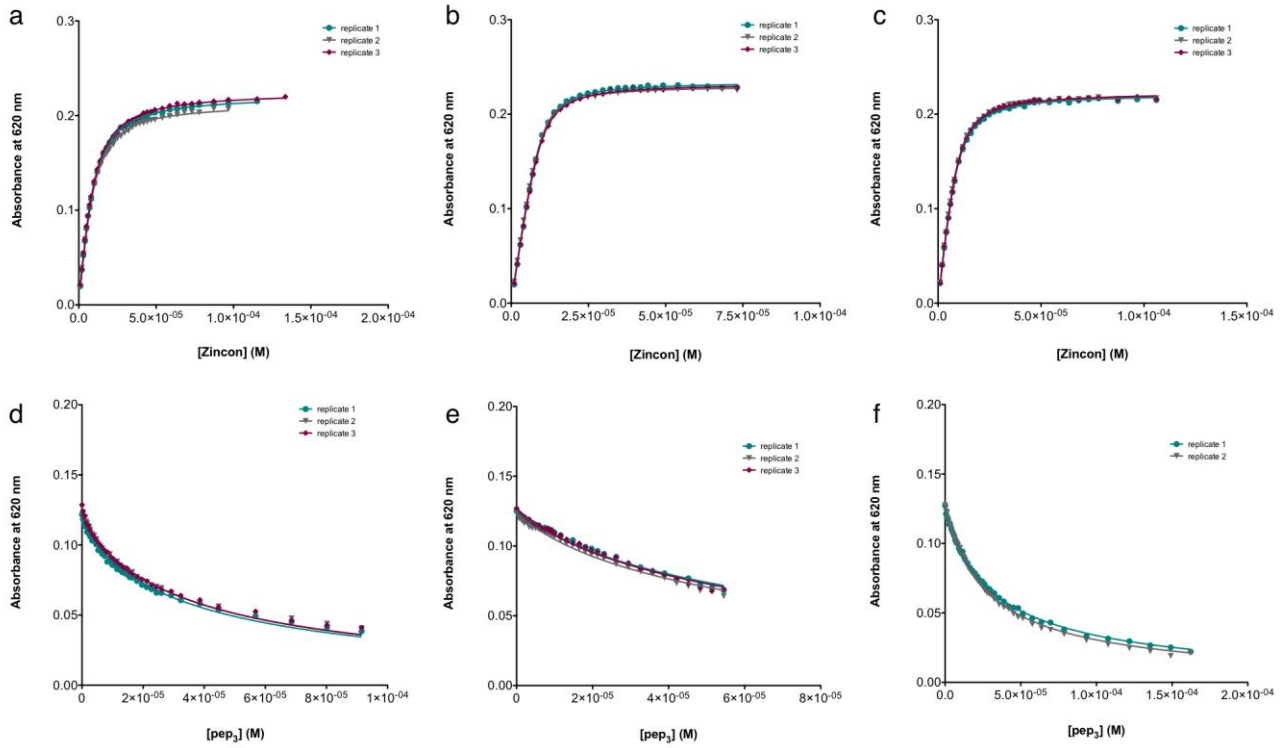

Figure S6. Competitive titrations against Zincon at pH 9.0 for (**TRI**L2WL23H)$_3$, [Hg(II)]$_S$(**TRI**L9HL23C)$_3^-$, and [Hg(II)]$_S$(**TRI**L9CL19H)$_3^-$. Plots of absorbances at 620 nm vs [Zincon] for the forward titrations of a) (**TRI**L2WL23H)$_3$, b) [Hg(II)]$_S$(**TRI**L9HL23C)$_3^-$, and c) [Hg(II)]$_S$(**TRI**L9CL19H)$_3^-$ and vs [pep$_3$] for the reverse titrations of d) (**TRI**L2WL23H)$_3$, e) [Hg(II)]$_S$(**TRI**L9HL23C)$_3^-$, and f) [Hg(II)]$_S$(**TRI**L9CL19H)$_3^-$.

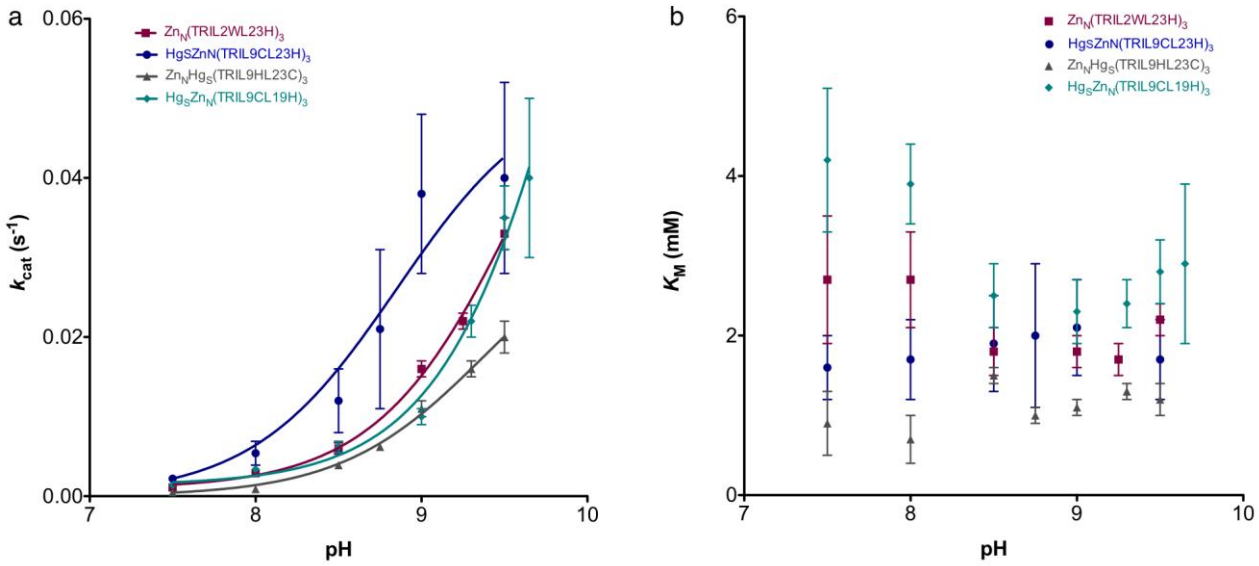

Figure S7. pH dependency of a) k_{cat} and b) K_M parameters for *p*NPA hydrolysis by Zn(II)His_3O sites in the **TRI** peptides. Results are shown for $[Zn(II)(H_2O/OH^-)]_N$(**TRI**L2WL23H)$_3^{n+}$, $[Hg(II)]_S[Zn(II)(H_2O/OH^-)]_N$(**TRI**L9CL23H)$_3^{n+}$,[1] $[Zn(II)(H_2O/OH^-)]_N[Hg(II)]_S$(**TRI**L9HL23C)$_3^{n+}$, and $[Hg(II)]_S[Zn(II)(H_2O/OH^-)]_N$(**TRI**L9CL19H)$_3^{n+}$. Error bars result from fitting all individual initial rates measured (three per concentration of substrate, without averaging) to the Michaelis-Menten equation in Prism 5 (GraphPad Software).

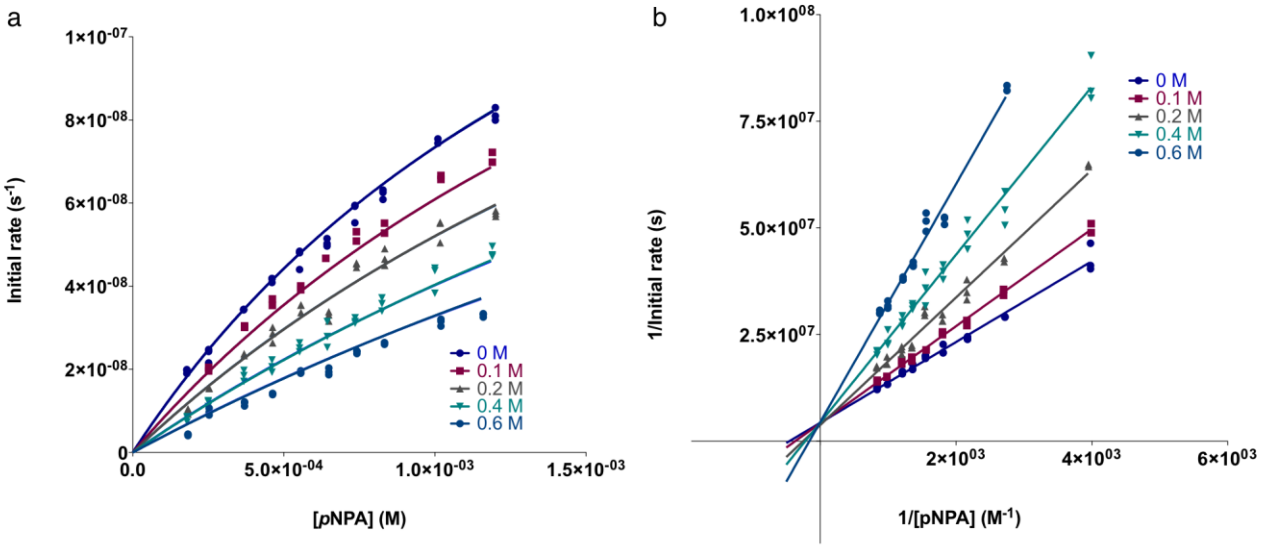

Figure S8. Inhibition of 20 μM $[Hg(II)]_S[Zn(II)(H_2O/OH^-)]_N$(**TRI**L9CL23H)$_3^{n+}$-catalyzed *p*NPA hydrolysis by acetate at pH 8.5. a) Initial rates as a function of substrate concentration in the presence of 0, 0.1, 0.2, 0.4, and 0.6 M potassium acetate fitted to a competitive inhibition model in Prism 5 (GraphPad Software). The global data yields the reported K_I and corresponding error. Data shown consists of each individual measured initial rate and does not represent averages. Fitting the same data to a mixed inhibition model yielded $\alpha \approx 14$ supporting the assignment of a competitive inhibition model.[2] b) Lineweaver-Burke (double-reciprocal) plots corresponding to the data in a). Visual inspection of the intersection of linear fits to each dataset (at the y-axis) also supports a competitive inhibition model.

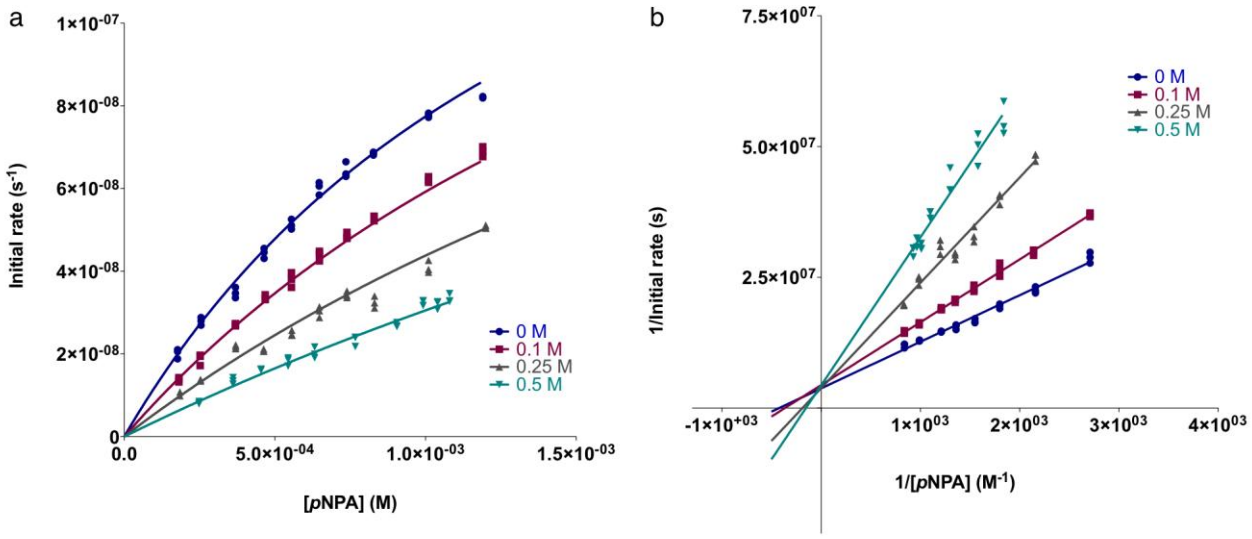

Figure S9. Inhibition of 50 μM [Zn(II)(H_2O/OH^-)]$_N$[Hg(II)]$_S$(**TRI**L9HL23C)$_3^{n+}$-catalyzed *p*NPA hydrolysis by acetate at pH 8.5. a) Initial rates as a function of substrate concentration in the presence of 0, 0.1, 0.25, and 0.5 M potassium acetate fitted to a competitive inhibition model in Prism 5 (GraphPad Software). The global data yields the reported K_I and corresponding error. Data shown consists of each measured individual initial rate and does not represent averages. Fitting the same data to a mixed inhibition model yielded $\alpha \approx 3 \times 10^{13}$ supporting the assignment of a competitive inhibition model.[2] b) Lineweaver-Burke (double-reciprocal) plots corresponding to the data in a). Visual inspection of the intersection of linear fits to each dataset (at the y-axis) also supports a competitive inhibition model.

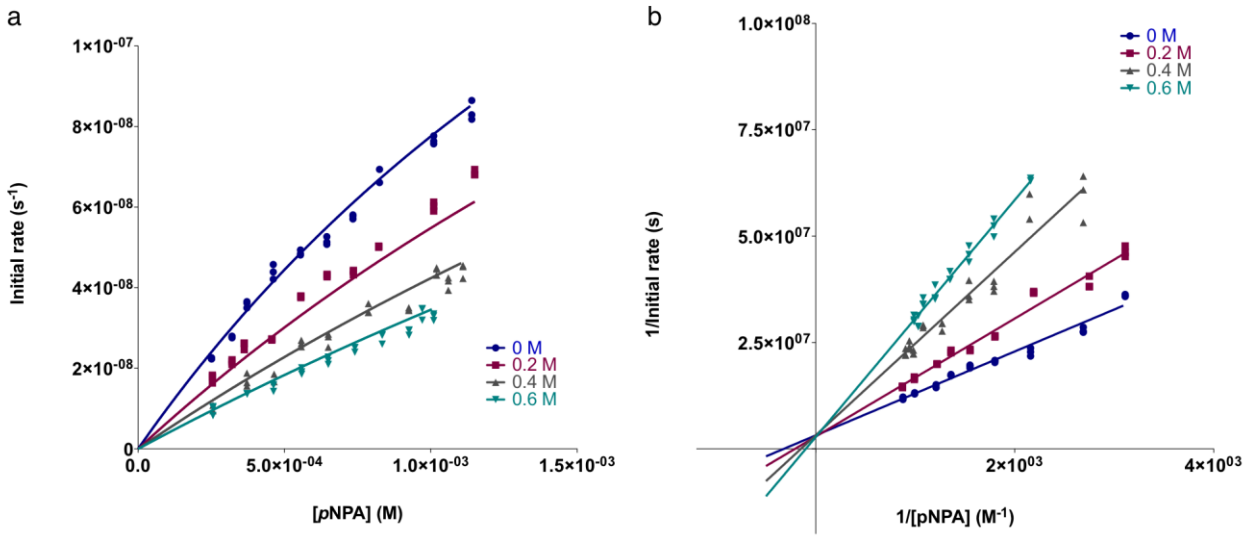

Figure S10. Inhibition of 50 μM $[Hg(II)]_S[Zn(II)(H_2O/OH^-)]_N$(**TRI**L9CL19H)$_3^{n+}$-catalyzed *p*NPA hydrolysis by acetate at pH 8.5. a) Initial rates as a function of substrate concentration in the presence of 0, 0.2, 0.4, and 0.6 M potassium acetate fitted to a competitive inhibition model in Prism 5 (GraphPad Software). The global data yields the reported K_I and corresponding error. Data shown consists of each measured individual initial rate and does not represent averages. Fitting the same data to a mixed inhibition model yielded $\alpha \approx 31$ supporting the assignment of a competitive inhibition model.[2] b) Lineweaver-Burke (double-reciprocal) plots corresponding to the data in a). Visual inspection of the intersection of linear fits to each dataset (at the y-axis) also supports a competitive inhibition model.

REFERENCES

(1) Zastrow, M. L.; Peacock, A. F. A.; Stuckey, J. A.; Pecoraro, V. L. *Nat. Chem.* **2012**, *4*, 118–23.

(2) Marangoni, A. G. *Enzyme Kinetics; reversible enzyme inhibition*; John Wiley & Sons, Inc.: Hoboken, NJ, USA, 2002; pp 61-69.